

# An Improved PDR/UWB Integrated System for Indoor Navigation Applications

Shuli Guo, Yitong Zhang, Xinzhe Gui, and Lina Han\*

**Abstract**—The challenges of the inertial navigation system based pedestrian dead reckoning (PDR) are mainly stochastic errors and serious accumulated errors caused by sensor variance, while the ultra-wideband (UWB) based positioning approaches are vulnerable to the external environment and produce many outliers under non-line-of-sight (NLOS) conditions. To overcome these shortcomings, this paper proposes a three-level improved PDR/UWB integrated system, in which the gait detection is first performed by a dual-frequency Butterworth filter, and the step length is accurately estimated based on a linear combination model. Then the position of the target is calculated by combining the step length and the heading information but calibrated periodically through the drift-free output of the UWB system. Finally, the noise distribution is dynamically adjusted through the NLOS assessment function, and the positioning accuracy is improved at information fusion level using the proposed variable noise variance Kalman filter. The positioning data is collected by our integrated small-scale sensors in both LOS and NLOS environments, and experiment results have demonstrated that the proposed PDR/UWB integrated system can significantly improve the accuracy of positioning information and can apply in indoor navigation applications.

**Index Terms**—integrated navigation system, pedestrian dead reckoning, ultra-wideband, Kalman filter.

## I. INTRODUCTION

INDOOR location-based services have attracted widespread attention in both academia and industry due to their huge commercial and social potential [1]-[3]. However, the indoor location is seriously affected by NLOS transmission channels between stations and receivers [4]. On account of the signal attenuation and multipath effect, global navigation satellite system signals are invalid or degraded in indoor environments where people spend the majority of their time [5].

The inertial navigation system (INS) is able to achieve self-contained navigation without extra infrastructure assistance. As a positioning method based on inertial sensors, PDR has the advantages of low cost, portable volume and strong autonomy [6]. Nevertheless, existing PDR solutions are still facing the

problem of cumulative errors due to the drift errors in inertial sensors and complex human activities. Therefore, reducing the accumulate errors in PDR system becomes more demandant as motivated by the need for accurate positioning information. From the PDR system itself, the mainstream approach to restrain the drift errors is to apply zero-velocity updates when the foot is stationary on the ground. This correction requires sensors to be mounted on the foot, and the foot-mounted sensors not only reduce the convenience and portability of the device, but also produce more complex gait features than shoulder when the carrier moves vigorously [7], [8]. The PDR system sets the data of inertial sensors as the input and achieves the navigation process through three parts of gait detection, step length estimation (SLE), and heading calculation, and pieces of research have been done on the improvement of these three parts [9]-[13].

### A. Gait Detection

Pedestrian distance walked is represented by the number of gait events, thus detecting steps accurately is a primary and crucial requirement for improving the positioning performance. Even if the estimation of step length is accurate, positioning errors can be extremely high due to inaccuracies in gait detection [14]. Among the typical gait detection approaches, threshold-based detection fails to find a unified way to detect steps by a simple threshold, template matching and spectral analysis rely too much on precise identifying periodicity in gait signals. It is difficult to use these algorithms to handle changes in walking speed and to eliminate false positives caused by any periodic movement within the expected frequencies [15], [16]. Whereas peak detection and zero crossings are popular choices to use the cyclic property to monitor the acceleration values. Kang proposed a peak step counting algorithm to mark the candidate stepping points of time that have the possibility of user walking and employed three judgments on acceleration to accurately detect the step event [17]. Ju used a first-order low pass filter with a cut-off frequency set to 5Hz and performed peak detection to detect a step accurately at a heel strike [18].

### B. Step Length Estimation

Two mainstream SLE models for calculating step length are models based on biological prior information and models based on data characteristics. The former models are established according to the mechanical nature of the human body, Zijlstra regarded leg behaviors as the inverted pendulum movement process and introduced the integral of vertical acceleration into a non-linear SLE model, which obtained good identifications of stride cycles and walking speed from the acceleration data [19]. Hu proposed a kinematic walking model that keeps the crucial

This work was supported in part by the National Key Research & Development Program of China under Grant 2017YFF0207400, in part by the National Center for Clinical Medical Research of Geriatric Diseases Fund Project under Grant NCRCG-PLAGH-2018009.

S. Guo, Y. Zhang, and X. Gui are with the State Key Laboratory of Intelligent Control and Decision of Complex Systems, School of Automation, Beijing Institute of Technology, Beijing 100081, China (e-mail: guoshuli@bit.edu.cn; zytjasper@163.com; guizinzhe@lowfet.com).

\*L. Han is with the Department of Cardiovascular Internal Medicine of Second Medical Center, Chinese PLA General Hospital, Beijing 100853, China (e-mail: hanlina9703@163.com). Asterisk indicates corresponding author.

characteristics of both the biped rolling-foot and the inverted pendulum model and enabled calibration of the parameters during walking using a 3D-accelerometer on the waist [20].

In the latter approach, Levi proposed a SLE model based on the linear relationship between step length and frequency [21]. Then the variance of acceleration, the amplitude of vertical acceleration and the statistical parameters of acceleration were introduced into the model to establish the correlation with the step length [22]. In addition, using intelligent algorithms to analyze the connection between data features and outputs is also a common method. Song regarded the features of acceleration as input to establish a multi-modal SLE neural network and judged the motion state of pedestrians through the proposed model [23]. Vathsangam proposed a speed estimation model based on the Gaussian regression training by setting the Fourier transform of acceleration and angular velocity as input and the walking speed as output [24]. Zihajezadeh set the modulus of external acceleration as the main feature in the Gaussian regression process, and further improved the accuracy of the speed estimation model [25].

### C. Heading Calculation

Applying the short-distance wireless sensor technologies to calibrate the positioning information in the PDR system is a mainstream heading calibration approach, including Zigbee [26], Bluetooth [27], UWB [28], wireless fidelity [29], and radio frequency identification [30]. The direct combination of wireless technologies and PDR could slightly improve the positioning accuracy since the accuracy degree of Bluetooth and radio frequency methods is meter-level. Meanwhile, UWB provides the centimeter-level distance between the tag and transmitting node by using the angle of arrival (AOA) and the time difference of arrival (TDOA) algorithms. And It has the advantages of high communication capacity, low transmission signal power spectral density, resistance to frequency-selective fading and efficient data transfer rate [31].

However, the UWB system is sensitive to channel fading and will generate a non-negligible number of outliers under NLOS conditions. The refresh rate of UWB is commonly between 10 Hz to 100 Hz, which means the independent UWB can barely obtain continuous ranging information, and its positioning results are irregular and volatile [32]. To suppress the influence of NLOS during the positioning process, interacting multiple model and classification algorithms including machine learning, support vector machine, and Gauss regression process were widely used to assess the NLOS state of UWB [33]-[35]. Wymeersch applied two classes of non-parametric regressors to form an estimate of the ranging error, and directly mitigated the bias incurred in both LOS and NLOS conditions [36]. Yang proposed a novel NLOS mitigation method based on sparse pseudo-input Gaussian process with low complexity and achieved comparable high performance in NLOS scenario [37].

The refresh rate of inertial sensors is much higher than UWB, accelerometers and gyroscopes can continuously characterize the motion intensity and attitude change of monitored target. The continuous output of PDR could favorably improve the positioning performance of integrated system [38]. Since PDR system provides continuous and accurate short-term trajectories, the drift-free output of UWB system can correct drift errors in PDR system. We could combine two systems to minimize the

aforementioned restricts associated with the standalone installation of PDR or UWB.

Meanwhile, Kalman filter is commonly used to establish the state equation of PDR and UWB fusion systems through the prior information on the covariance matrix of data [39]-[41]. But the Kalman filter algorithm critically relies on the accurate system model and statistical distribution of noises, and has not considered the outliers in UWB systems caused by environmental effects. Li improved the robust fusion of UWB and PDR based on the extended Kalman filter, and the Mahalanobis distance from the observation to the prior distribution is used to suppress the influence of abnormal UWB data [42], [43]. Xu provided real time estimation by performing an unbiased finite impulse response filter bank algorithm to correct the difference between the INS-measured and UWB-measured position [44]. However, the dynamic performance of the existing positioning system fails to satisfy the practical applications under NLOS conditions [45].

The practical application of this paper is to design a two-dimensional positioning system for the security guards, aiming to expand the positioning function of existing security communication system under NLOS conditions by adding the proposed PDR/UWB integrated system. We first investigate the independent use of PDR system to further improve the positioning accuracy, and then optimizes the PDR/UWB integrated structure. We propose a dual-frequency Butterworth filter for accurate gait detection, and establish a linear combination SLE model with multiple features. The L-nearest neighbor gradient descent algorithm is performed to achieve a fast estimation of parameters in the model. The proposed integrated system uses the drift-free heading of UWB to calibrate the accumulated errors in real time. Then we construct a NLOS assessment function based on Gauss distribution to evaluate the transmission attenuation of signals, and a variable noise variance Kalman filter is proposed by dynamically adjusting noise distribution according to the NLOS conditions.

In summary, this paper enhances the fusion of PDR and UWB system as follows:

- Step length is estimated accurately based on the proposed state transition diagram and the linear combination model. The heading direction of PDR system are calibrated periodically by UWB in real time thus the integrated system can quickly calculate the precise navigation trajectory. There are few constraints on the choice of moving targets, thus the independence between the users and integrated system is achieved.
- A NLOS assessment function is proposed to calculate the probability of signal attenuation based on the prior assumption that the received signal strength conforms to the Gauss distribution. The proposed variable noise variance (VNV) Kalman filter effectively relieves the dependence of integrated system on the statistical distribution of noises, and the accurate navigation in an indoor environment with NLOS conditions is achieved.
- We integrated INS and UWB modules on a 3 cm × 4.26 cm circuit board using a high-speed processor with a 32-bit ARM Cortex-M4, and a portability-driven integrated positioning system has been achieved.

The organization of this paper is as follows. Section II describes the general framework of the integrated positioning

system in detail. In Section III, some improved PDR algorithms and the hybrid indoor navigation method based on VNV Kalman filter are proposed. Section IV presents the hardware implementation and experimental results under LOS/NLOS environments. Finally, conclusions and future works are summarized in section V.

## II. SYSTEM FRAMEWORK

The block diagram of the improved PDR/UWB integrated positioning system is presented in Fig. 1. The inertial sensor module consists of a tri-axial accelerometer, a tri-axial gyroscope, and a tri-axial magnetometer, the UWB module consists of a location tag and three base stations.

As it can be seen in Fig. 1, the original data of acceleration, angular velocity, and orientation are collected by inertial measurement units and transformed by a rotation matrix. Afterwards, the number and length of steps are accurately estimated based on the proposed dual-frequency Butterworth filter and multi-feature linear combination model. The UWB system performs trilateration methods between tag and three base stations to measure position and attitude of carriers. Based on the periodic heading calculation function, the heading directions of PDR are limited to a stable range and calibrated periodically by the drift-free output of the UWB through joint calibration. Meanwhile, the parameters of multi-feature linear combination model are real-time estimated by performing the gradient descent algorithm based on the positioning information of the UWB system. Aiming at indoor navigation applications, a NLOS condition assessment function is proposed based on the Gaussian distribution of the outliers. Setting the positioning information of UWB as measurement values, the output of PDR system is fused by the VNV Kalman filter where the noise distribution is dynamically adjusted through the NLOS assessment function. The improved PDR/UWB integrated positioning system provide accurate positioning information and robust fusion strategies for indoor navigation applications.

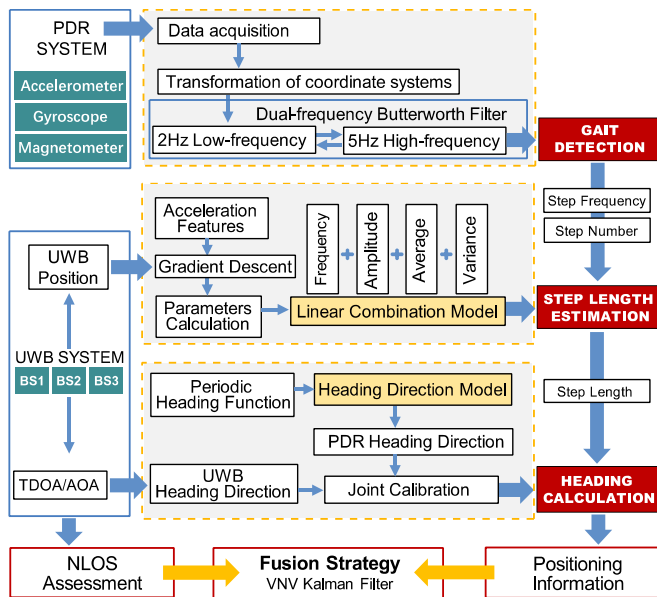


Fig. 1. General block diagram of the PDR/UWB combined system

## III. PROPOSED METHOD

### A. State Transition in Gait Detection

The modulus of acceleration contains periodic features that can be used to describe the pedestrian motion and achieve gait detection. However, the acceleration modulus is sensitive to the mounting position of sensors and show distinct features under different movements. Performing attitude algorithms to transform the acceleration data from sensor coordinate system (SCS) to earth coordinate system (ECS) could obtain continuous and stable results. The transformation process between the coordinate systems is defined by:

$$(\alpha_{Ex}, \alpha_{Ey}, \alpha_{Ez}) = C_E^S \cdot (\alpha_{Sx}, \alpha_{Sy}, \alpha_{Sz}) \quad (1)$$

where  $(\alpha_{Ex}, \alpha_{Ey}, \alpha_{Ez})$  and  $(\alpha_{Sx}, \alpha_{Sy}, \alpha_{Sz})$  are the acceleration data under ECS and SCS, respectively.  $C_E^S$  is the rotation matrix from SCS to ECS.

The acceleration direction after performing the attitude algorithm is always consistent with the human motion, ignoring the installation position of the sensors, which provides a guarantee for accurately extracting the statistical characteristics of the acceleration. Since the accelerometer is sensitive to minute vibrations, filtering the acceleration data could minimize or even eliminate the interference in the signal. We first perform the 2Hz and 5Hz Butterworth low-pass filter on the same set of acceleration signal respectively, and the comparison is shown in Fig. 2.

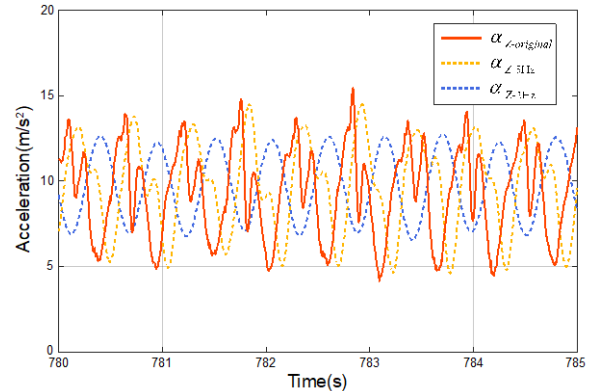


Fig. 2. Comparison of filtered signals between 2Hz/5Hz Butterworth filter

We observe that the low-frequency filter effectively removes the fake peaks and valleys, but misses amount of data features and produces large delays from the original signal. Whilst the high-frequency filter completely preserves the acceleration data characteristics during walking, but leaves multiple peaks and valleys in each cycle, resulting in the failure of gait detection. In order to eliminate the delay after signal filtering and extract real features, we propose a dual-frequency combined Butterworth filter of 2-Hz and 5-Hz. The peaks and valleys of each cycle are firstly obtained by a 2 Hz low-frequency filter, and then the real peaks and valleys are searched retrospectively in the 5 Hz high-frequency filtered signal based on these features.

The low-frequency and high-frequency filtered signals of vertical acceleration are expressed as  $a_{Lfc}$  and  $a_{Hfc}$ , and the peak moments are  $T_{Lf}^{peak}(k)$  and  $T_{Hf}^{peak}(k)$ , respectively. Therefore, the backtracking process for real peaks and valleys based on the dual-frequency filter is described as (see Fig. 3) :

$$\begin{cases} T_{Hf}^{peak}(k) = \arg \max_t (a_{Hf}(t)), & T_{Lf}^{peak}(k-1) < t < T_{Lf}^{peak}(k) \\ T_{Hf}^{valley}(k) = \arg \min_t (a_{Hf}(t)), & T_{Lf}^{peak}(k-1) < t < T_{Lf}^{peak}(k) \end{cases} \quad (2)$$

where  $\arg \max$  is the set of arguments, for which  $a_{Hf}(t)$  attains the largest value in the interval  $T_{Lf}^{peak}(k-1)$  to  $T_{Lf}^{peak}(k)$ .

As can be seen from Fig. 3, the backtracking process first obtains the peaks of  $(k-1)_{th}$  and  $k_{th}$  step from low-frequency filtered signals, and then regards the maximum and minimum acceleration between  $T_{Lf}^{peak}(k-1)$  and  $T_{Lf}^{peak}(k)$  as the peak and valley of high-frequency filtered signals at time moment  $k$ . Moreover, the features of the first step are all included in the previous cycle of the first peak. Therefore, before detecting the peaks, it is necessary to constantly detect the valleys to obtain complete peak and valley information of the first step.

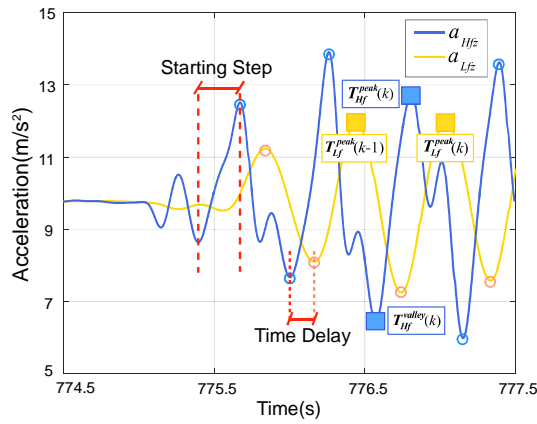


Fig. 3. Backtracking process for real peaks and valleys based on proposed dual-frequency Butterworth filter

In order to accurately represent the transition relationship between gait states, we propose the flow chart of peak-to-valley gait state detection as shown in Fig. 4.

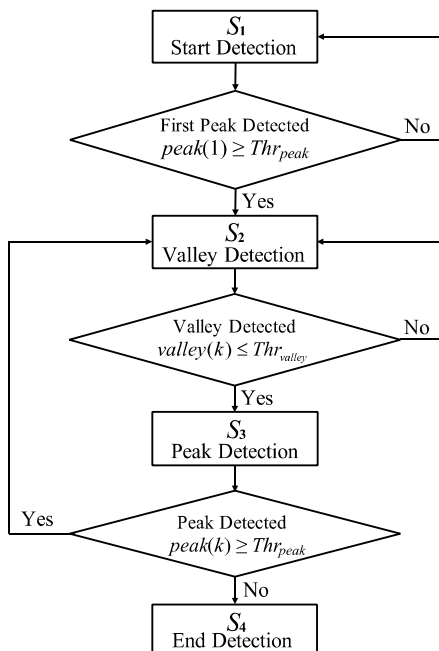


Fig. 4. The flow chart of Peak-to-valley gait state detection

During the state of S1, the first peak of acceleration is detected to determine whether pedestrians start walking or not, and constant start detection could ensure the features of the first step are completely detected. Once the first peak is extracted, the valleys will be continually detected during the state of S2, and the whole cycle of each step is detected within the state of valley detection and peak detection by setting a peak threshold  $Thr_{peak}$  and a valley threshold  $Thr_{valley}$ . When a peak smaller than  $Thr_{peak}$  is detected after valleys, it indicates that the current walking process is over and should return to the S1 state again to wait for the next start detection.

### B. Linear Combination of Step Length Model

Although biomechanical models provide simplicity and acceptable performance, accelerometers are often required to be installed as close as possible to the center of mass, which greatly limits the mounting position of sensors. Based on biological experience, the variety of step length is directly reflected in the statistical features of acceleration. Weinberg proposed the model (3) and indicated that the step length is proportional to the amplitude of vertical acceleration within a step cycle [46]. Scarlett proposed the model (4) and took into account the distribution of acceleration, solving the problem of spring during the step [47]. Moreover, Shin proposed the model (5) and established the relationship between step length, step frequency, and acceleration variance [22].

$$SL_{wb}(k) = \alpha_1 \cdot \sqrt[4]{A_{max}(k) - A_{min}(k)} \quad (3)$$

$$SL_{sc}(k) = \alpha_1 \cdot \frac{\bar{A}(k) - A_{min}(k)}{A_{max}(k) - A_{min}(k)} \quad (4)$$

$$SL_{sh}(k) = \alpha_1 \cdot f(k) + \alpha_2 \cdot \delta(k)^2 + \alpha_3 \quad (5)$$

where  $A_{max}(k)$  and  $A_{min}(k)$  are the maximum and minimum values of vertical acceleration within the  $k$  step, respectively.  $\alpha_1$ ,  $\alpha_2$ , and  $\alpha_3$  are constants set to convert the unit scale, and  $\bar{A}(k)$  represents the average value of acceleration within the  $k$  step,  $f(k)$  is the step frequency, and  $\delta(k)^2$  is the variance of acceleration within the  $k$  step.

However, single features could not fully characterize the step length. We add step frequency, amplitude, mean and variance of acceleration into the SLE model, and propose a linear combination model with multiple features as follows:

$$S(k) = \rho_1 f(k) + \rho_2 \sqrt[4]{A_{max}(k) - A_{min}(k)} + \rho_3 \frac{\bar{A}(k) - A_{min}(k)}{A_{max}(k) - A_{min}(k)} + \rho_4 \delta^2(k) + \rho_5 = \langle \rho, f \rangle \quad (6)$$

where  $\rho = [\rho_1, \rho_2, \rho_3, \rho_4, \rho_5]$  are weight coefficients of features,  $f = [F_{1k}, F_{2k}, F_{3k}, F_{4k}, F_{5k}]$ , and  $\delta(k)^2 = \sum_{i=1}^{N(k)} [A_i(k) - \bar{A}(k)]^2 / [N(k) - 1]$ .

Existing SLE model pre-collects the data samples of pedestrian walking at a fixed distance and then estimates the specific parameters of the model offline. Such offline model has high estimation accuracy but is highly limited by data samples, resulting in low scalability and robustness. Therefore, we calculate the parameters of the linear combination SLE model in real time by constructing the online metric function of

L-nearest steps. The function selects the nearest  $L$  steps to quantify the difference between the target step length and calculated step length, and is set as follows:

$$J(k) = \sum_{i=k-L+1}^k |T(i) - S(i)|^2, \quad k > L \quad (7)$$

where  $T(i)$  is the target length of the  $k_{th}$  step and  $S(i)$  is the step length calculated by SLE models. During the offline estimation,  $T(i)$  is set as the average step length of fixed distance, and during the online estimation,  $T(i)$  is set as the step length estimated by UWB in real time.

We construct a flow sample group containing  $L$  samples and perform the gradient descent on the whole flow sample group after each step estimation. The real-time estimation of parameters using the gradient descent method is described as follows:

$$\rho_i(k) = \rho_i(k-1) - \alpha \cdot \frac{\partial J(k)}{\partial \rho_i} \quad (8)$$

$$\frac{\partial J(k)}{\partial \rho_i} = -\frac{2}{L} \sum_k^{k+L} (T(k) - S(k)) \frac{S(k)}{\partial \rho_i} \quad (9)$$

where  $\rho_i(k)$  and  $\rho_i(k-1)$  represent the coefficient values of the  $i_{th}$  feature at time moment  $k$  and  $k-1$ ,  $\alpha$  is the learning rate used to control the speed of descent, equation (9) calculates the direction in which the gradient descends the fastest.

### C. Calibration of Heading Direction

Gyroscopes could measure carrier attitude change, but the output heading is affected by bias instability and accumulates a serious drift with regard to time. At the same time, the magnetometer is not able to provide accurate direction under the indoor environment with strong magnetic interferences, resulting in an abnormal heading direction that cannot be aligned with the true heading angle under ECS. For the above problem, we use the drift-free output of UWB to suppress the bias instability in the PDR system and provide an accurate heading reference to achieve the heading alignment of PDR system. In order to avoid the discontinuous sudden change of angle between two adjacent steps during walking, we limit the angle difference within  $2\pi$  interval and establish a periodic heading calibration function as follows:

$$\psi(k) = \begin{cases} \psi(k-1) + \Delta\psi(k) + 2\pi & \Delta\psi(k) < -\pi \\ \psi(k-1) + \Delta\psi(k) & -\pi \leq \Delta\psi(k) \leq \pi \\ \psi(k-1) + \Delta\psi(k) - 2\pi & \Delta\psi(k) > \pi \end{cases} \quad (10)$$

where  $\Delta\psi(k)$  represents the angle difference between two adjacent steps and is defined as:  $\Delta\psi(k) = \psi(k) - \psi(k-1)$ .

The output heading direction of the PDR system includes not only the real heading angle, but also the inherent drift and fixed angle deviation when aligning the coordinate system. We propose a joint calibration model of heading direction based on the above periodic heading calibration function as follows:

$$\begin{cases} \psi_{PDR}^*(k) = \psi_{real}(k) + \psi_p + \psi_{drift}(k) + n_p \\ \psi_{UWB}^*(k) = \psi_{real}(k) + \psi_u + n_u \end{cases} \quad (11)$$

where  $\psi_{PDR}^*(k)$  and  $\psi_{UWB}^*(k)$  represent the output heading direction of PDR and UWB systems, respectively.  $\psi_{real}(k)$  is

the real heading angle and  $\psi_{drift}(k)$  is the inherent drift of the PDR system.  $\psi_p$  and  $\psi_u$  stand for angle deviations of the PDR and UWB systems, respectively.  $n_p$  and  $n_u$  are white noise with a mean of zero.

The difference of heading direction between UWB and PDR systems is defined as:

$$\begin{aligned} E(k) &= \psi_{UWB}^*(k) - \psi_{PDR}^*(k) \\ &= \psi_p - \psi_u + \psi_{drift}(k) + (n_p - n_u) \end{aligned} \quad (12)$$

When aligning the coordinate system of PDR to the UWB system, we consider the heading angle deviation  $\psi_u$  of UWB system to be 0, and set the inherent drift to a linear function related to the gyroscope zero-offset, which is obtained by:

$$\psi_{drift}(k) = gyro_{offset} \cdot t(k) \quad (13)$$

Hence the difference of heading direction could be simplified and expressed as:

$$E(k) = \psi_p + gyro_{offset} \cdot t(k) + (n_p - n_u) \quad (14)$$

where  $gyro_{offset}$  denotes the gyroscope zero-offset which is approximately constant in a short period of time. Therefore, the difference  $E(k)$  is regarded as a linear function of time  $t(k)$ . In order to achieve real-time heading calibration, we construct the metric function based on L-nearest neighbor samples as:

$$M(k) = \sqrt{\sum_{i=k-L+1}^k |E(i)|^2}, \quad k > L \quad (15)$$

We notice that a large number of neighbor samples can effectively reduce the impact of noise on the estimation results, and obtain accurate model parameters, but also increase the computational burden and speed down the real-time estimation process. The maximum number of samples should be selected according to the performance requirements and computing capability of the embedded sensors in the practical application.

### D. NLOS Evaluation Based on Gaussian Distribution

NLOS occurs when any obstacles disrupt the transmission of wireless signals. Signals obtained at the receiver in the NLOS environment contain bias errors and generate a large number of outliers, resulting in serious degradation or even invalidation of positioning accuracy. Various methods for identifying and evaluating the extent of NLOS have been proposed [10-12], but the linear discriminant model based on exact threshold or piecewise function lacks of theoretical results and unable to specifically characterize the degree of real NLOS environment.

When obstacles disrupt the transmission of signals, part of the received signals strength (RSS) are weakened by obstacles and then arrive at the receiver along the straight line, on the other hand, the signals arrive at the receiver after multiple reflections. We denote the RSS which first reaches the receiver along the straight line as  $RSS_{FP}$ , and set the real received as  $RSS_R$ , which includes  $RSS_{FP}$  and other signal strengths that arrive at the receiver after multiple reflections [48]. The difference between  $RSS_{FP}$  and  $RSS_R$  is defined as follow:

$$\Delta RSS = RSS_R - RSS_{FP} \quad (16)$$

The value of  $\Delta RSS$  the degree to which the signal strength is weakened by obstacles when transmitted along the straight line,

which reflects the NLOS level between base stations and tags. According to the conclusion in [49], when the difference of RSS exceeds an upper threshold  $Thr_U$ , indicating that the received signal is significantly attenuated during transmission, and is in the NLOS conditions with great probability. On the contrary, when the  $\Delta RSS$  less than a lower threshold  $Thr_L$ , representing that the signal is slightly distorted and is in the NLOS conditions with minimal probability. And the above process can be described as:

$$\begin{cases} P_{NLOS}(\Delta RSS > Thr_U) = 1 - \delta_1 \\ P_{NLOS}(\Delta RSS < Thr_L) = \delta_2 \end{cases} \quad (17)$$

where  $\delta_1, \delta_2$  are the adaptive confidence levels set in advance and subjected to  $\delta_1, \delta_2 \in (0, 0.05)$ .

We assume that  $\Delta RSS$  follows the Gaussian distribution with a mean of  $\mu$  and a variance of  $\sigma^2$ , and could be expressed as  $\Delta RSS \sim N(\mu, \sigma^2)$ .

$$\begin{cases} P_{NLOS}(\frac{\Delta RSS - \mu}{\sigma} \geq k_U) = 1 - \delta_1 \\ P_{NLOS}(\frac{\Delta RSS - \mu}{\sigma} \leq k_L) = 1 - \delta_1 \end{cases} \quad (18)$$

where  $k_U$  and  $k_L$  are the standard normal random variables, representing the values of the cumulative normal distribution at  $1 - \delta_1$ . And the threshold can be obtained by:

$$\begin{cases} Thr_U = \sigma k_U + \mu \\ Thr_L = \sigma k_L + \mu \end{cases} \quad (19)$$

Suppose  $\mu$  is equal to the average of  $Thr_U$  and  $Thr_L$ , the mean  $\mu$  and variance  $\sigma^2$  could be expressed as:

$$\begin{cases} \mu = \frac{1}{2}(Thr_U + Thr_L) \\ \sigma = \frac{Thr_U - Thr_L}{k_U - k_L} \end{cases} \quad (20)$$

Based on the above assumptions and derivations, the degree of NLOS between tag and base stations could be specifically assessed in terms of probability density function by:

$$P[\Delta RSS(k)] = \int_{-\infty}^{\Delta RSS(k)} \frac{1}{\sigma\sqrt{2\pi}} e^{-\frac{(x-\mu)^2}{2\sigma^2}} dx \quad (21)$$

The UWB system based on the trilateration methods has three independent base stations A1, A2, and A3. We set **A**, **B**, and **C** as three independent events that represent each base station is affected by NLOS conditions. The overall degree of NLOS conditions at the moving target can be assessed according to the independent events by:

$$\begin{aligned} P_{Total}(k) &= P(\mathbf{A} \cup \mathbf{B} \cup \mathbf{C}) \\ &= 1 - P(\bar{\mathbf{A}} \cap \bar{\mathbf{B}} \cap \bar{\mathbf{C}}) \\ &= 1 - P(\bar{\mathbf{A}}) \cdot P(\bar{\mathbf{B}}) \cdot P(\bar{\mathbf{C}}) \\ &= 1 - [1 - P(\mathbf{A})][1 - P(\mathbf{B})][1 - P(\mathbf{C})] \end{aligned} \quad (22)$$

### E. System Fusion Using VNV Kalman Filter

Existing Kalman filter algorithms have not considered the outliers caused by NLOS environment. Setting the process noise and measurement noise to constant cannot accurately describe the noise distribution during transmission. We respectively set PDR system as the state equation and UWB system as the measurement equation, the state equation is periodically corrected according to the output of UWB in real time. Starting from the state  $X(k-1)$  at previous step with the evolution rules described by the state transition matrix  $A$  and responding to the inputs  $u(k)$  with the evolution matrix  $B$ . We define the state equation as follows to describe the evolution of system state according to Kalman filter principles.

$$X(k) = AX(k-1) + Bu(k-1) + q(k-1) \quad (23)$$

where  $A$  and  $B$  are considered as identity matrix, and  $k$  represents a new pedestrian step.  $X(k) = [x(k) \ y(k)]^T$  denotes the position state vector of the moving target at step  $k$ , and  $q(k-1)$  denotes the process noise vector at step  $k-1$  which models the uncertainty of state dynamics with covariance matrix  $Q$ , and the system input  $u(k-1)$  is set as:

$$u(k-1) = \begin{bmatrix} S(k) \cdot \cos \psi_{PDR}^*(k-1) \\ S(k) \cdot \sin \psi_{PDR}^*(k-1) \end{bmatrix} \quad (24)$$

The measurement equation is set as follows according to the UWB system:

$$Z(k) = HX(k) + r(k) \quad (25)$$

where  $Z(k) = [x_{UWB}(k) \ y_{UWB}(k)]^T$  denotes the output position of UWB system and is taken as observation values at step  $k$ .  $H$  represents the measurement matrix and is considered as identity matrix.  $r(k)$  denotes the measurement noise vector at step  $k$  which models the uncertainty of measurement dynamics with covariance  $R$ .

The variance distribution of the measurement noise and process noise is dynamically adjusted using the proposed NLOS assessment function according to the degree of outliers. And we establish the relationship between measurement noise, process noise, and NLOS assessment function as follows:

$$R(k) = P_{Total}(k) \cdot R_0 \quad (26)$$

$$Q(k-1) = [1 - P_{Total}(k-1)] \cdot Q_0 \quad (27)$$

We set the measurement noise variance in x and y orientation to  $\sigma_{Rx}^2$  and  $\sigma_{Ry}^2$ , and the process noise variance to  $\sigma_{Qx}^2$  and  $\sigma_{Qy}^2$ , respectively. The initial values of measurement covariance matrix  $R_0$  and process covariance matrix  $Q_0$  are defined as follows:

$$Q_0 = \begin{bmatrix} \sigma_{Qx}^2 & 0 \\ 0 & \sigma_{Qy}^2 \end{bmatrix} \quad R_0 = \begin{bmatrix} \sigma_{Rx}^2 & 0 \\ 0 & \sigma_{Ry}^2 \end{bmatrix} \quad (28)$$

Based on the above description, we replace the fixed value of process noise and measurement noise with variable noise variance during the fusion process, and propose a novel fusion strategy of the integrated system using VNV Kalman filter as shown in Fig 5.



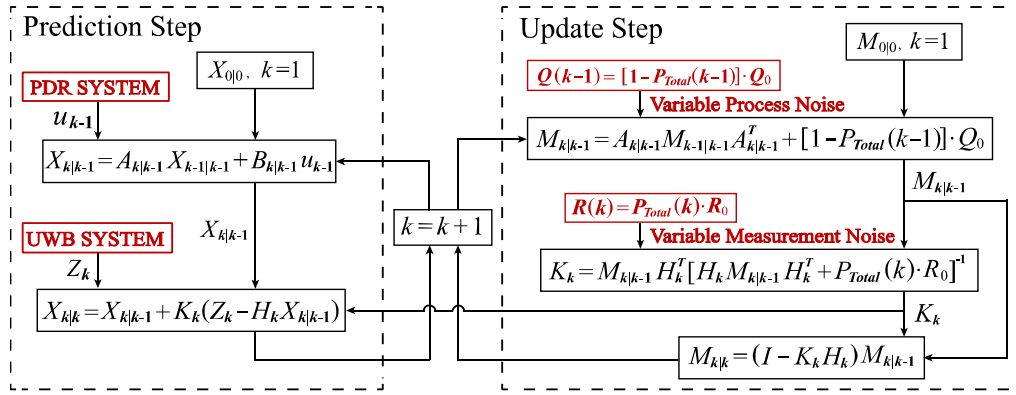


Fig. 5. VNV Kalman filter principle of the PDR/UWB integrated system

We predict the current state of integrated system given the previous measurements, and establish the predict equation of Kalman filter as follows:

$$\begin{cases} X_{k|k-1} = A_{k|k-1} X_{k-1|k-1} + B_{k|k-1} u_{k-1} \\ M_{k|k-1} = A_{k|k-1} M_{k-1|k-1} A_{k|k-1}^T + [1 - P_{Total}(k-1)] \cdot Q_0 \end{cases} \quad (29)$$

where  $X_{k|k-1}$  and  $M_{k|k-1}$  denotes the priori state estimate and priori covariance matrix of the state vector, respectively, at step  $k$  before obtaining the measurement. Similarly, we update the predicted state given the current measurement, and establish the update equation of Kalman filter as follows:

$$\begin{cases} K_k = M_{k|k-1} H_k^T [H_k M_{k|k-1} H_k^T + P_{Total}(k) \cdot R_0]^{-1} \\ X_{k|k} = X_{k|k-1} + K_k (Z_k - H_k X_{k|k-1}) \\ M_{k|k} = (I - K_k H_k) M_{k|k-1} \end{cases} \quad (30)$$

where  $X_{k|k}$  and  $M_{k|k}$  respectively represent the posteriori state estimate and posteriori covariance matrix of the state vector at step  $k$  after obtaining the measurement, and  $K_k$  is the Kalman gain. We provide a summarized version of the VNV Kalman filter by Algorithm 1.

#### Algorithm 1 Variable Noise Variance Kalman Filter

**Input:**  $A_{k|k-1}$ ,  $H_k$ ,  $\delta_1$ ,  $\delta_2$ ,  $Q_0$  and  $R_0$ ,

**Output:**  $X_{k|k}$

- 1:  $X_{0|0} = E\{X_0\}$ ,  $M_{0|0} = E\{X_0 X_0^T\}$
- 2: **for**  $k = 1$  **to**  $N$  **do**
- 3: Assess the total NLOS value  $P_{Total}(k)$  according to Eq. (21):

$$P(A) = P[\Delta RSS_{A1}(k)] = \int_{-\infty}^{\infty} \frac{1}{\sigma \sqrt{2\pi}} e^{-\frac{(x-\mu)^2}{2\sigma^2}} dx \quad (31-1)$$

$$P(B) = P[\Delta RSS_{A2}(k)] = \int_{-\infty}^{\infty} \frac{1}{\sigma \sqrt{2\pi}} e^{-\frac{(x-\mu)^2}{2\sigma^2}} dx \quad (31-2)$$

$$P(C) = P[\Delta RSS_{A3}(k)] = \int_{-\infty}^{\infty} \frac{1}{\sigma \sqrt{2\pi}} e^{-\frac{(x-\mu)^2}{2\sigma^2}} dx \quad (31-3)$$

- 4: Calculate measurement noise  $R(k)$  and process noise  $Q(k)$  according to Eq. (26) and Eq. (27)
- 5: Prediction Step:

$$X_{k|k-1} = A_{k|k-1} X_{k-1|k-1} + B_{k|k-1} u_{k-1} \quad (32-1)$$

$$M_{k|k-1} = A_{k|k-1} M_{k-1|k-1} A_{k|k-1}^T + [1 - P_{Total}(k-1)] \cdot Q_0 \quad (32-2)$$

- 6: Update Step:

$$r_k = Z_k - H_k X_{k|k-1} \quad (33-1)$$

$$S_k = H_k M_{k|k-1} H_k^T + P_{Total}(k) \cdot R_0 \quad (33-2)$$

$$K_k = M_{k|k-1} H_k^T S_k^{-1} \quad (33-3)$$

$$X_{k|k} = X_{k|k-1} + K_k r_k \quad (33-4)$$

$$M_{k|k} = (I - K_k H_k) M_{k|k-1} \quad (33-5)$$

7: Return  $X_{k|k}$  and  $M_{k|k}$

8:  $k = k + 1$

9: **end for**

## IV. EXPERIMENTS AND RESULTS

### A. Experimental Setup

The block diagram of the improved PDR/UWB integrated system is displayed in Fig.6. The practical application of this paper is to design a positioning system for the security guards, which can be easily mounted on the shoulder of moving target through the strap or baldric, and the wearable devices are powered by the portable power sources. The antennas of base stations are fixed at a height similar to the pedestrian using tripods. In the process of positioning, the accelerometer, gyroscope, and magnetometer communicate with the microcontroller unit (MCU) based on I2C protocol. The entire integrated system achieves data exchange through the wireless network. Afterwards, all data processing and fusion tasks are completed on the host computer which has an Intel® Core™ i5-7300 CPU with a 2.5GHz clock.

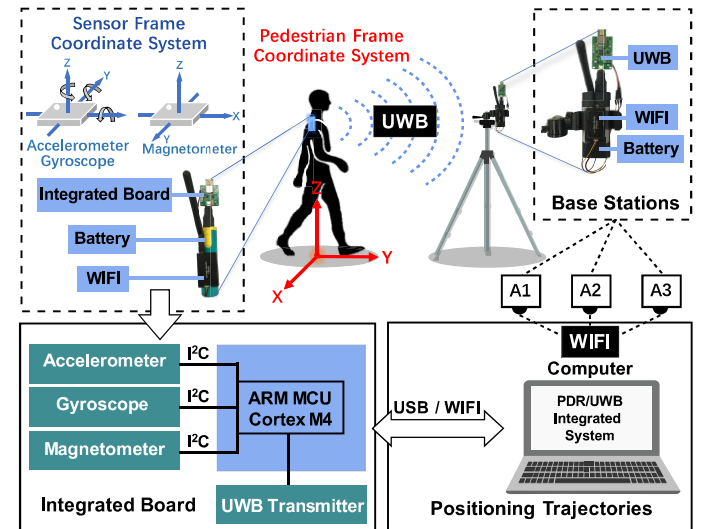


Fig. 6. Block diagram of the PDR/UWB integrated principle

In order to improve the portability of PDR/UWB integrated system and ensure the minimum volume while having satisfied accuracy and sufficient transmission rate, we integrated the 3D-accelerometer and 3D-gyroscope of ICM20602 module, the 3D-magnetometer of IST8310 module and the UWB wireless positioning nodes of DWM1000 module with three base stations based on the high-speed processor STM32F405 using a 32-bit ARM CortexM4. The schematic circuit rendering and printed circuit board of the PDR/UWB integrated system are presented in Fig. 7. The sampling frequency of inertial sensors is 200Hz, which could provide continuous trajectory information and preserve the completely original signal of motion without relying on any other equipment in three-dimensional space. Meanwhile, DWM1000 wireless positioning sensors provides the centimeter-level accuracy at high transmission rates with a refresh rate of 20 Hz. The

performance parameters of the PDR/UWB integrated system we designed are summarized in Table I.

All LOS experiments involving PDR system were performed in the outdoor environment shown in Fig. 8(a), whereas the NLOS related experiments were performed in the indoor environment shown in Fig. 8(b). We only consider the slightly mixed situation of LOS and short-term NLOS, where the UWB signal is blocked in a short period of time by the columns. The yellow circle represents the location of the moving target, the black arrow represents the moving trajectory, the gray square represents the column, and the white triangle represents three base stations. Prior to the start of the experiment, all the sensors had been basically calibrated, and the moving target would stay in place for 5 seconds at the beginning of the walk to perform the initial alignment of inertial sensors.

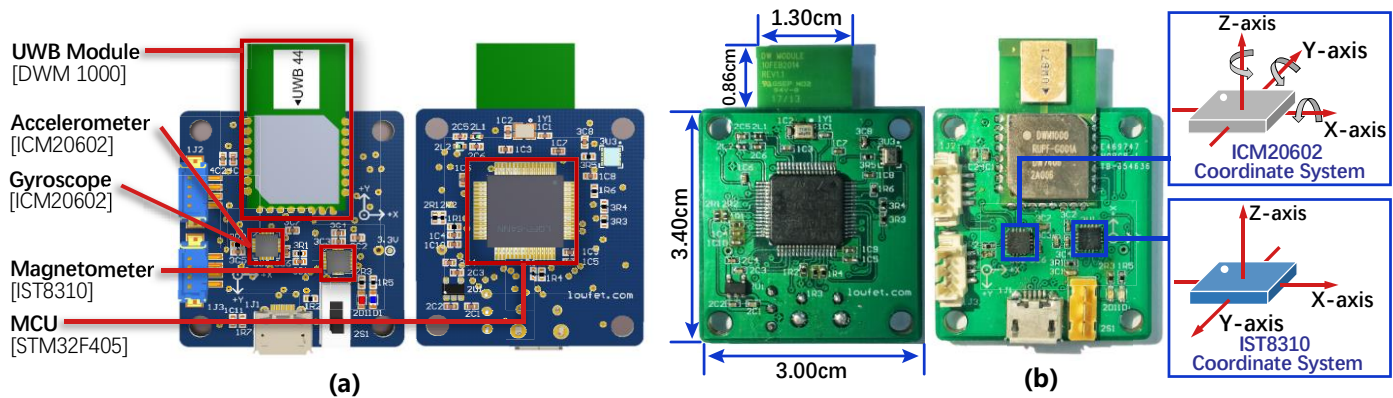


Fig. 7. Circuit Board of the PDR/UWB integrated system

(a) The schematic diagram and printed wire layout (b) Printed circuit board and coordinate system of inertial sensors

TABLE I  
PERFORMANCE PARAMETERS OF INERTIAL SENSORS

Parameter	Accelerometer	Gyroscope	Magnetometer
Noise	$100\mu g / \sqrt{Hz}$	$\pm 4mdps / \sqrt{Hz}$	$\pm 0.1\%FS$
Full Range scale	$\pm 16g$	$\pm 2000dps$	X / Y : $\pm 1600uT$ Z : $\pm 2500uT$
Voltage Range	1.71V-3.45V	1.71V-3.45V	1.72V-3.6V
Zero-Rate Output	X / Y : $\pm 0.5mg/^{\circ}C$ Z : $\pm 1mg/^{\circ}C$	$\pm 0.01dps/^{\circ}C$	$\pm 0.024uT/^{\circ}K$
Initial Tolerance	$\pm 40mg$	$\pm 1dps$	$\pm 0.3uT$
Interface	400 kHz I2C	400 kHz I2C	400 kHz I2C

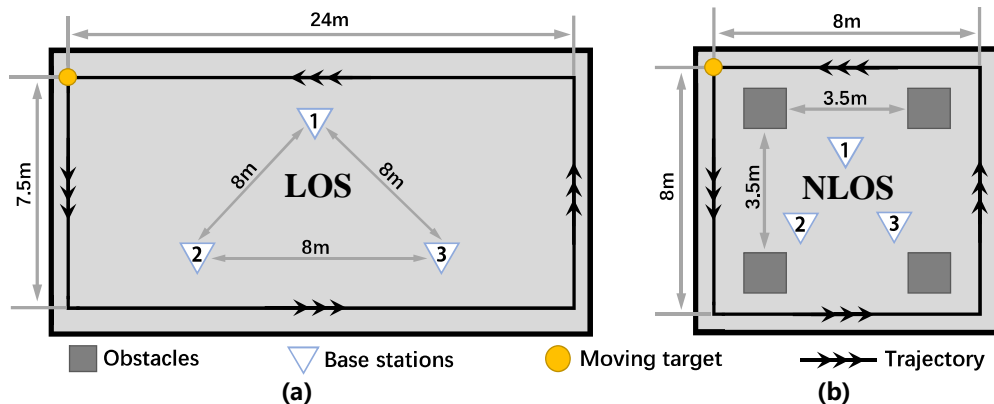


Fig. 8. Experiment site and node deployment

(a) Outdoor environment under LOS condition, (b) Indoor environment under NLOS condition



### B. Number-of-Steps Detection

Since the human walking frequency is concentrated at 0.5 Hz to 5 Hz and the walking speed ranges from 0.5m/s to 3.5m/s. Based on the state transition diagram, we set the value of the dual-frequency Butterworth filter to 2 Hz and 5 Hz and performed gait detection on the data collected from uniform walking. The dual-frequency Butterworth filter was applied to detect peaks and valleys as shown in Fig. 9. We observe that the backtracking process not only avoids fake peaks and valleys but also eliminates the time delay caused by the filtering process.

The gait features of pedestrian are highly correlated with walking speed and direction. To further verify the robustness of the proposed state transition diagram under various gait features, we set the fixed number of target steps to 50, 80, 120, 200 and performed following four experiments on the targets of different gender: walk straight at normal speed, walk straight at normal speed, walk straight at random speed and walk in random direction at random speed. The measured number of steps was counted in Table. II.

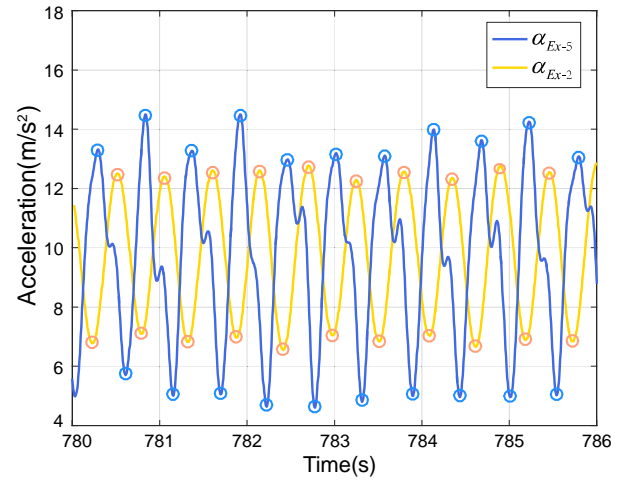


Fig. 9. Detection of single peaks and valleys

TABLE II  
STATISTICAL RESULTS OF GAIT DETECTION

Case Description	Target	Detected steps/Target steps (Errors)			
		1 <sup>st</sup> Test	2 <sup>nd</sup> Test	3 <sup>rd</sup> Test	4 <sup>th</sup> Test
Speed: 0.5-1.5 m/s Direction: Straight	Male	50/50(0%)	80/80(0%)	119/120(-0.83%)	202/200(+1%)
	Female	49/50(-2%)	80/80(0%)	121/120(+0.83%)	201/200(+0.5%)
Speed: 2-3.5 m/s Direction: Straight	Male	50/50(0%)	80/80(0%)	120/120(0%)	200/200(0%)
	Female	50/50(0%)	80/80(0%)	119/120(-0.83%)	199/200(0%)
Speed: Random Direction: Straight	Male	50/50(0%)	80/80(0%)	120/120(0%)	198/200(-1%)
	Female	50/50(0%)	79/80(-1.25%)	120/120(0%)	201/200(+0.5%)
Speed: Random Direction: Random	Male	51/50(+2%)	80/80(0%)	121/120(+0.83%)	202/200(+1%)
	Female	51/50(+2%)	78/80(-2.5%)	122/120(+1.67%)	202/200(+1%)

The statistical results in Table II indicate that the instability of walking speed and direction will increase the number of fake peaks and valleys, and the gait features of pedestrian are more obvious when walking straight at a constant speed. The proposed state transition diagram could obtain accurate and robust gait detection results for different moving targets in most scenarios, but the detection accuracy will be slightly affected by the excessively low speed and substantially sharply sudden change of direction. The fake peaks will appear in the signal filtered at 2Hz low frequency when walking excessively slow, resulting in the miss detection of the target feature points. When the moving target walks randomly on the ground with multiple obstacles, abnormal gait such as step turns, spin turns and pace changes will lead to multiple fake peaks and valleys within a walking cycle.

### C. Parameter Estimation of SLE Models

For the proposed linear SLE model, we set the initial value of gradient descent as  $\rho_1=\rho_2=\rho_3=\rho_4=\rho_5=1$ , and set the number of neighbor samples as  $L=50$ . An L-nearest neighbor gradient descent method was performed on 50 flow samples after each step estimation has completed. The convergence of the fitness function and parameters are presented in Fig. 10, which denotes

that the function converges within four steps and quickly obtains the parameters of current sample group. The estimation results also tend to be stable in the subsequent processes.

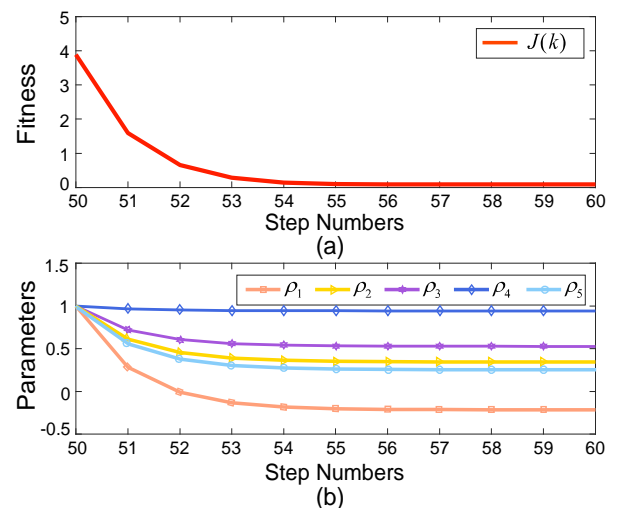


Fig. 10. (a) Convergence of the fitness function  
(b) Convergence of parameters in the linear combination model

TABLE III  
RESULTS AND ERRORS OF WALKING DISTANCE ESTIMATION USING DIFFERENT SLE MODELS

Test	Walking Distance(m)	Weinberg Model(m)	Scarlett Model(m)	Shin Model(m)	Inverted Pendulum Model(m)	Linear Combination Model(m)	Neural Network Fitting(m)
1	15.35	15.53 (+1.17%)	15.23 (-0.78%)	15.12 (-1.50%)	16.44 (+7.10%)	15.14 (-1.37%)	15.29 (-0.39%)
2	15.52	15.45 (-0.45%)	15.39 (-0.84%)	15.30 (-1.42%)	16.39 (+5.61%)	15.19 (-2.13%)	15.35 (-1.10%)
3	17.17	17.10 (-0.41%)	18.39 (+7.11%)	17.52 (-2.04%)	16.43 (-4.31%)	17.15 (-0.12%)	16.40 (-4.48%)
4	19.92	19.18 (-3.71%)	18.55 (-6.88%)	19.58 (-1.71%)	18.23 (-8.48%)	19.33 (-2.96%)	19.69 (-1.15%)
5	20.19	19.15 (-5.15%)	18.80 (-6.88%)	19.27 (-4.56%)	18.60 (-7.88%)	19.48 (-3.52%)	20.04 (-0.74%)
Errors		<b>2.18%</b>	<b>4.50%</b>	<b>2.25%</b>	<b>6.68%</b>	<b>2.02%</b>	<b>1.57%</b>

To further validate the advantages of the proposed SLE model, we performed the least squares algorithm to estimate parameters in the Weinberg model, the Scarlett model, and the Shin model and calculated the nonlinear parameters of models by using particle swarm optimization. In addition, a five-input feedback SLE neural network was designed with gait features as inputs and step length goals as reference values. The walking distance was calculated based on the SLE models mentioned above, and the averages of the difference between calculated distance and actual distance were considered as the distance error. The relevant results are summarized in Table III.

The estimation errors indicate that the accuracy of the Scarlett model and inverted pendulum model is poor and the maximum error in the short distance test reaches 8.48%, which seriously affects the output of the PDR system. Our proposed linear combination SLE model involves a variety of gait features and achieves relatively accurate estimation results compared with other experiments. However, the model with multiple features also increases the dependence of the model on the accurate calculation of gait features, the error estimation of any features will directly lead to the failure of step length estimation. Although the feedback SLE neural network could further improve the accuracy of estimation results, it is highly correlated with the training samples and has a large computational burden, which makes it difficult to operate on portable devices with limited computational power.

In a word, using the proposed L-nearest neighbor gradient descent to establish the real-time linear combination model with multiple gait features could achieve the step length estimation with satisfactory accuracy and efficiency.

#### D. Joint Calibration of Heading

Since the UWB system provides a higher sampling rate with respect to the walking steps, we merely use the UWB position between two adjacent steps to compute the heading direction based on the peaks and valleys. According to equation (10), we transformed the output of PDR and UWB systems into constant values using the proposed periodic heading calibration function, and obtained the constant angles as shown in Fig.11(a).

Then we used the drift-free output of UWB system to calibrate heading direction by the joint calibration model in order to eliminate the drift errors in PDR system. Since the heading angle difference between two systems  $E(k)$  is regarded

as a linear function of time, we first performed the least squares algorithm to solve the parameters of metric function constructed in equation (15) in real time. The parameters in least square method were set to have the following values:

$$A = \begin{bmatrix} \varphi(k-L) \\ \varphi(k-L-1) \\ \vdots \\ \varphi(k) \end{bmatrix} \quad Y = \begin{bmatrix} E(k-L) \\ E(k-L-1) \\ \vdots \\ E(k) \end{bmatrix} \quad (34)$$

$$\varphi(k) = [1 \quad t(k)] \quad X = [\psi_p \quad gyro_{offset}]^T \quad (35)$$

After obtaining the coefficients  $\psi_p$  and  $gyro_{offset}$  of heading angle difference in the  $k-1$  step, the calibrated angle  $\psi_{PDR}^*(k)$  of the  $k$  step is calculated using the proposed joint calibration model according to equation (11) and present the calibrated heading angles of PDR system in Fig. 11(b).

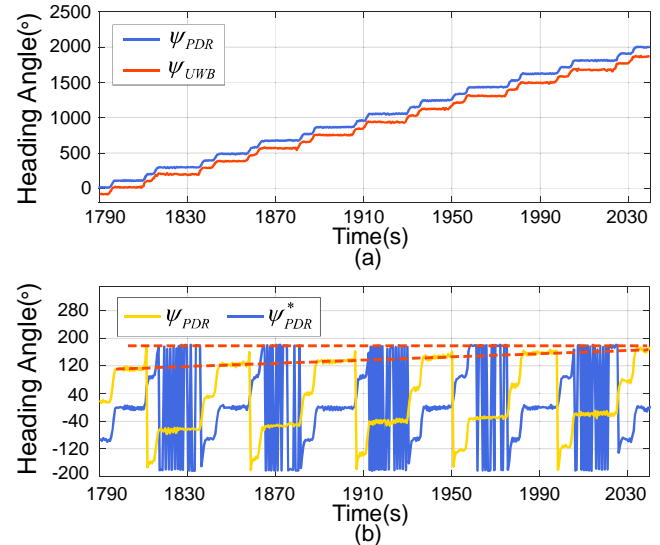


Fig. 11. (a) Transformed constant heading angles of integrated system  
(b) Comparison of calibrated heading angles of PDR system

We observe that the drift errors caused by the successive integration of gyroscope leads to an increasing trend of the uncalibrated heading angles under same conditions, and produces an obvious deviation of nearly 60 degrees after

walking for five laps. Meanwhile, the calibrated heading angles represented by the blue lines in Fig. 11(b) is constant for 5 laps, verifying the stability of the heading output from the proposed periodic heading calibration function and joint calibration model. Then we combined the calibrated heading direction with the step length obtained from the linear combination model to perform the dead reckoning, and the comparison of positioning trajectories using uncalibrated and calibrated heading direction was presented in Fig. 12 and Fig. 13.

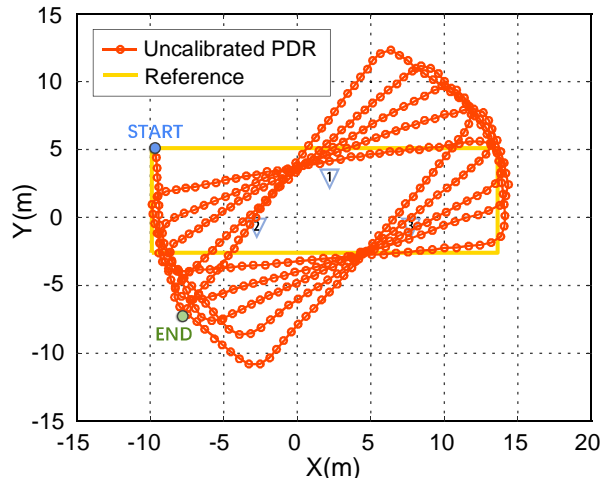


Fig. 12. Positioning trajectories using uncalibrated heading direction

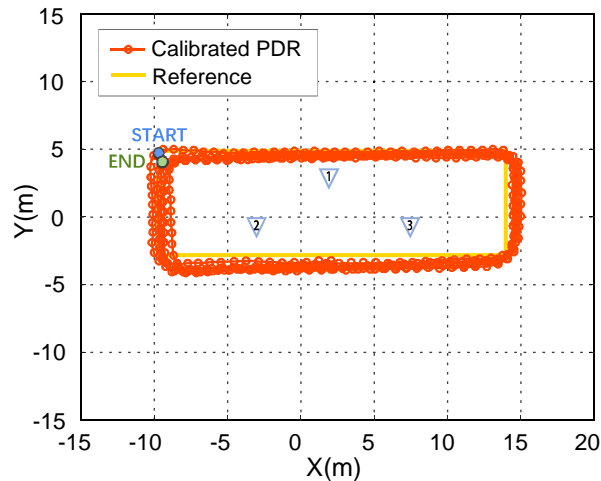


Fig. 13. Positioning trajectories using calibrated heading direction

The positioning trajectories using uncalibrated heading direction have deviated substantially from the reference path, and does not terminate near the starting point due to the distortion of the heading angles. Meanwhile the calibrated heading direction almost eliminates the drift errors accumulated over time and the dead reckoning results obtained by using the corrected angles significantly improves the accuracy of the positioning system. The navigation results of Fig. 12 and Fig. 13 validate that the proposed periodic heading calculation function and the joint calibration model could effectively eliminate the drift errors of PDR system and obtain accurate positioning information.

To further compare the performance of the models involved

in section IV.C, we let the moving target walk more five turns in the open environment as shown in Fig. 8(a). By combining the step length calculated by each model with the calibrated heading angles, we presented the comparison of positioning results obtained by different dead reckoning models in Fig. 14. Then we calculate the position deviations based on the coordinate differences of the trajectory breakpoints, and consider the maximum, minimum and average value of position deviations as the evaluation indicator. Furthermore, since the real walking distance differs from the predefined trajectory, we calculate the average of the different estimated values of the same step in the five circles, and regard them as a relative reference path. The relative error is defined as the Euclidean distance between the positioning results and the relative reference path, so as to independently reflect the regression degree of positioning results without referring the real walking distance. The position error comparison of different SLE models is summarized in Table IV.

TABLE IV  
POSITION ERROR COMPARISON OF DIFFERENT SLE MODELS

	Maximum error(m)	Average error(m)	Minimum error(m)	Relative error(m)
Weinberg	2.448	1.002	0.005	0.895
Scarlett	3.596	1.704	0.009	1.435
Shin	2.401	1.068	0.005	0.997
Inverted pendulum	5.389	2.854	0.008	2.376
Proposed	0.985	0.326	0.001	0.341
Neural Network	2.554	1.072	0.004	1.921

We observed from the positioning results of each model that the trajectory calculated by the inverted pendulum model seriously deviated from the reference trajectory and it could hardly perform a reliable dead reckoning process, which was consistent with the conclusion drawn in the previous section. The Weinberg model and the Shin model obtained the relatively accurate trajectories, but the deviation of the positioning results accumulated over time due to the continuous recursion process in pedestrian dead reckoning. Fig. 14(e) indicate that the linear combination model could obtain the best dynamic positioning performance compared with other SLE models, and the level of the average error demonstrated that the obtained positioning trajectory was almost completely coincident with the reference route in five laps. In addition, the feedback neural network obtained accurate step length in the previous section, but the neural network SLE model seriously relies on the specific training samples, which significantly reduced the generalization of the static positioning performance, making it difficult to calculate the trajectory of various samples in real time.

The experimental results draw a conclusion that the proposed linear combination model merely accumulates an average error of 0.326 meters after long distance walking, and reaches the best static positioning performance among other SLE models. The proposed model contains abundant gait features, which effectively lessens the dependence of step length estimation results on any single parameters.

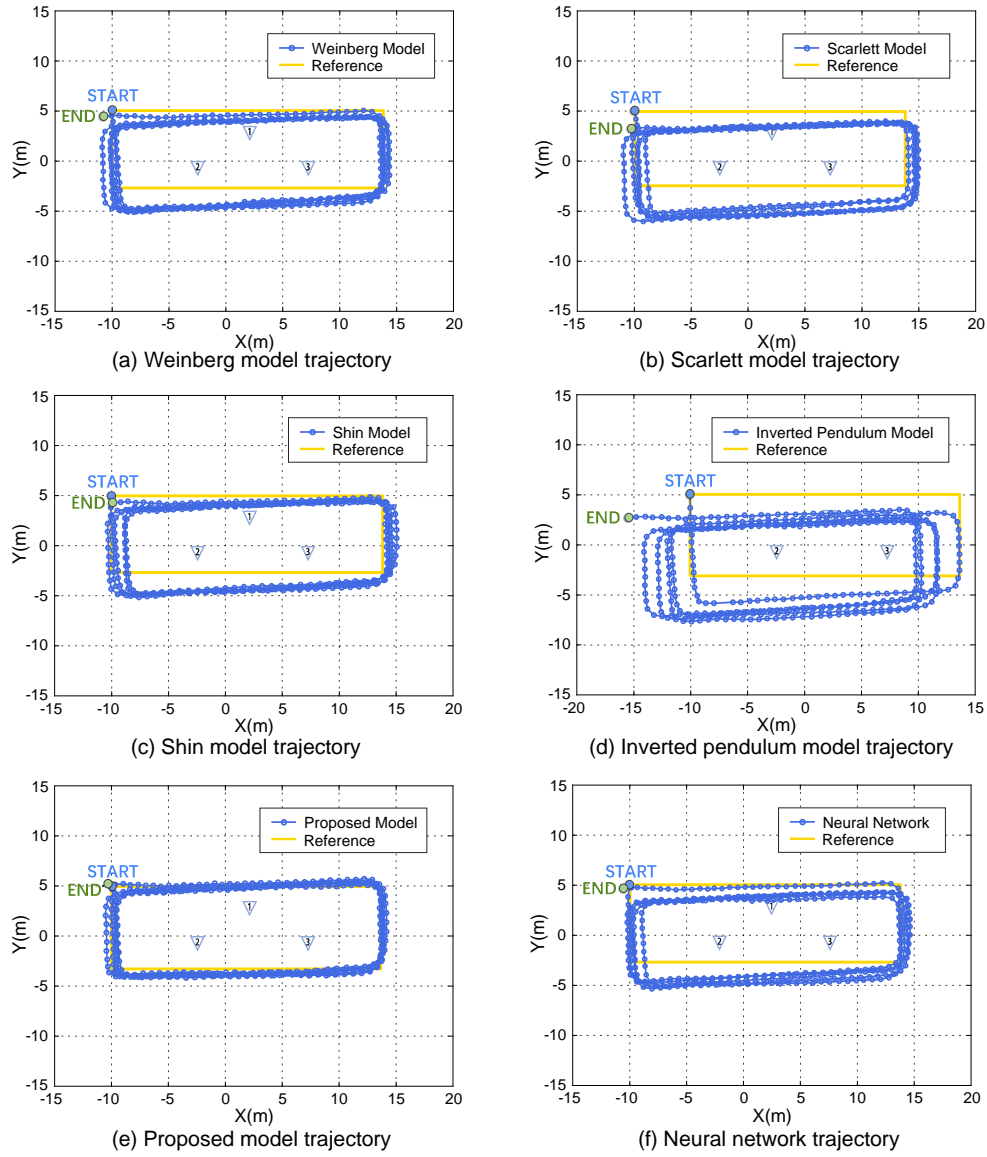


Fig. 14. Positioning results under different SLE models  
(a) Weinberg model (b) Scarlett model (c) Shin model (d) Inverted pendulum model (e) Linear combination model (f) Neural network

### E. Positioning Experiments under NLOS Conditions

Before starting the experiments under NLOS conditions, we let the moving target randomly walk for 2 laps in the open environment as shown in Fig. 8(a) and used the obtained walking data to calculate the parameters of linear combination model and joint calibration model. Then we collected data of the target walking 2 more laps in the NLOS environment as shown in Fig. 8(b). We first set the adaptive confidence levels as  $\delta_1 = \delta_2 = 0.01$ , and define the measurement noise variance in x and y orientation as  $\sigma_{R_x}^2 = \sigma_{R_y}^2 = \sigma_R^2$ , and the process noise variance to  $\sigma_{Q_x}^2 = \sigma_{Q_y}^2 = \sigma_Q^2$ , respectively. Since the fusion results of Kalman filter algorithm seriously depends on the statistical distribution of noises, we compare the fusion results under different noise distribution by controlling the ratio between  $\sigma_Q^2$  and  $\sigma_R^2$ . When the process noise variance exceeds the measurement noise variance, the fusion result is more inclined to be modified by

the observation of UWB system. But if the measurement noise variance exceeds the process noise variance, the prediction of PDR system will dominate the fusion process. According to reference [50], we also add a switching mechanism to further improve the robustness of proposed integrated system during the long-term misalignment of UWB signals. We set  $Thr_M = 0.5$  as the signal misalignment threshold and consider that the system has lost the UWB signal when the value of  $P[\Delta RSS(k)]$  exceeds  $Thr_M$ . At this time, only the PDR signal is used to perform the trajectory positioning process. When the degree of NLOS  $P[\Delta RSS(k)]$  weakens to less than  $Thr_M$ , the UWB signal is fused again by the VNV Kalman filter algorithm to correct the PDR trajectory with large accumulation errors.

We performed the Kalman filter algorithm and switching mechanism to fuse the PDR and UWB systems and the ratio was set to be 10, 1, and 0.1, respectively, and the comparison of positioning trajectories under different ratios was shown in the

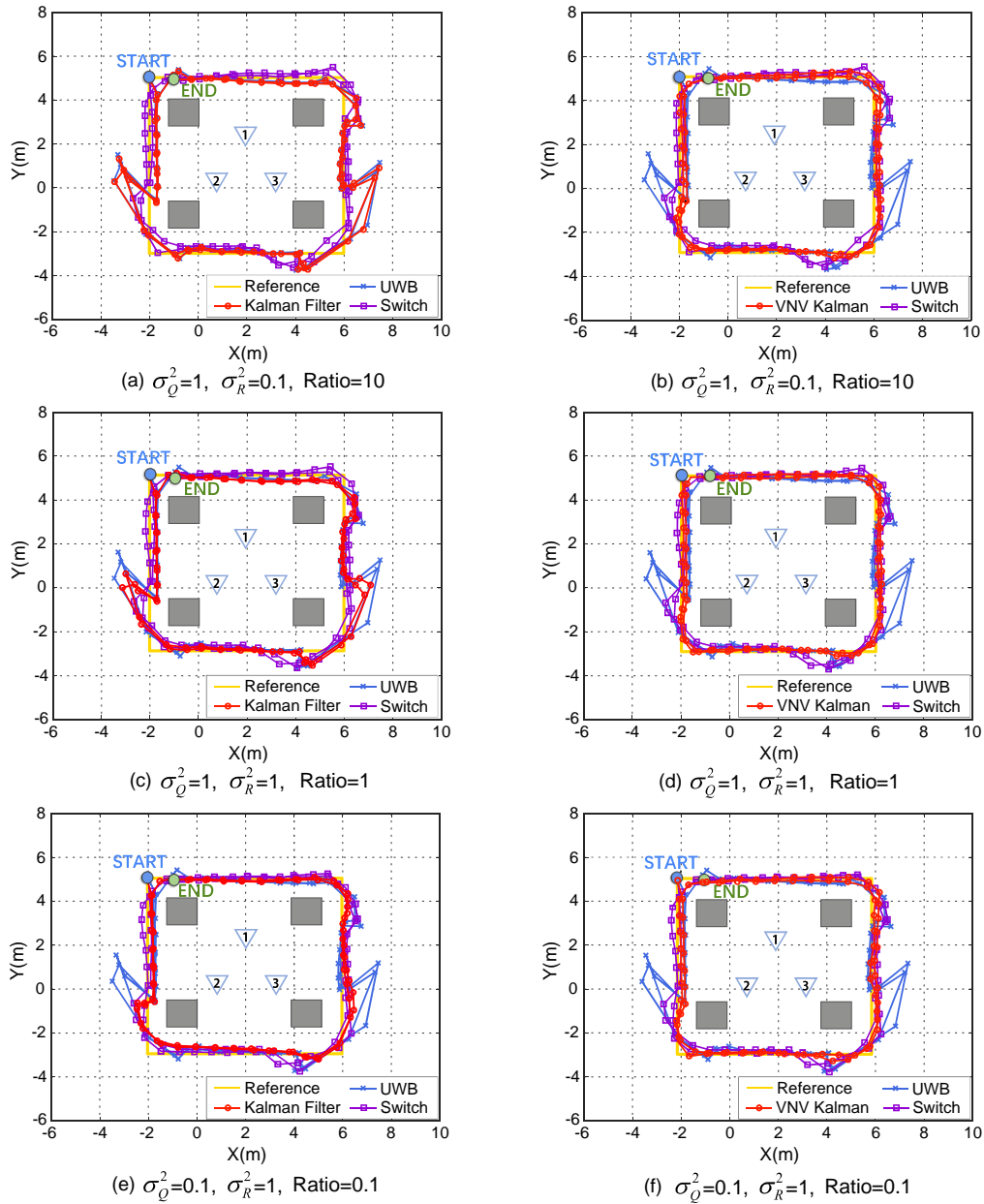


Fig. 15. Comparison of positioning trajectories using variable noise Kalman filter and traditional Kalman filter with different ratios between  $\sigma_Q^2$  and  $\sigma_R^2$

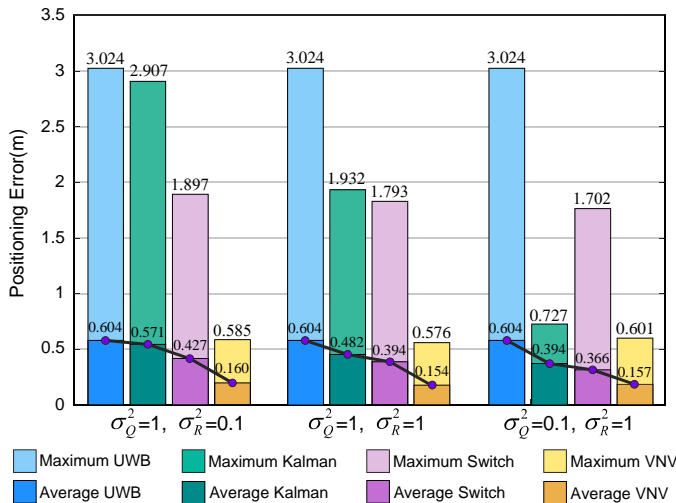


Fig. 16. Position errors comparison between Kalman filter and VNV filter

left side of Fig. 15. Then we performed the proposed VNV Kalman filter and switching mechanism to fuse PDR and UWB systems under the same parameters and conditions, and presented the positioning trajectories in the right side of Fig. 15. The maximum and average position errors of UWB, typical Kalman filter, switching mechanism and proposed VNV filter are summarized in Fig. 16.

As it can be seen in Fig. 15, from the blue positioning trajectories obtained by using UWB system independently, we observe that when the pedestrian passes through the column, the signal transmission will be seriously affected by NLOS conditions, resulting in a large positioning error as shown in Fig. 16. The red positioning trajectories in the left side of Fig. 15 indicates that using traditional Kalman filter algorithm can partly improve the similarity between the positioning result and reference trajectory, and the three maximum errors of Kalman filter in Fig. 16 also points out that the reduction of the ratios between the process noise variance and the measurement noise



variance can alleviate the influence of NLOS and improve the accuracy of positioning results. However, the fluctuations in three graphs also indicates that the erroneous observations caused a large drift in the Kalman update process, and the positioning results deviated significantly from the reference trajectory. The reduction of the ratio will enhance the dependence of the fusion system on the prediction process, and lead to the increase of cumulative error in the positioning results. Moreover, the precise noise ratio of the specific system is hard to obtain in practical applications, and the dependence of the algorithm on the noise distribution still exists, which limits the extensibility and real-time performance of the positioning system. The results of the switching mechanism indicate that UWB signals could quickly correct the accumulation offset during LOS and slight NLOS conditions, and reduce the average error of trajectories compared to traditional Kalman filter. However, the purple positioning trajectories calculated by using switching mechanism still produced an obvious offset during the switching phase.

The experimental results of the proposed VNV filter demonstrate that the improved PDR/UWB integrated system obtains an average error less than 0.160 meters, which is a considerable improvement compared with the existing methods in short-term NLOS environment [3], [28], [51], [52]. The improved positioning trajectories obtained almost coincide with the reference route, indicating that the negative influence of outliers under slight NLOS environment on the positioning performance was significantly eliminated. Moreover, the fusion results of proposed variable noise Kalman filter did not change with the ratios between the process noise variance and the measurement noise variance, which proved that the way of dynamically adjusting the noise variance according to the degree of NLOS effectively reduced the dependence of the integrated system on the statistical distribution of noises, and could provide an efficient structure for the real-time integration of fusion system in practical application. However

## V. CONCLUSION

In this paper, an improved PDR/UWB integrated system based on VNV Kalman filter algorithm was proven to be able to accurately provide pedestrian locations in indoor environments. The first contribution refers to inertial sensors is complete gait detection based on the dual-frequency Butterworth filter and the multi-feature linear combination model involving the step frequency, the amplitude of acceleration, the average of acceleration, and the variance of acceleration. The second contribution refers to UWB is that we use the positioning information of UWB system to estimate parameters of linear combination model in real time based on the L-nearest neighbor gradient descent method. And we use the drift-free heading direction of UWB to calibrate the heading angle of PDR processed by the periodic heading calculation function.

In the improved PDR/UWB integrated structure, UWB system plays a crucial role in terms of system position accuracy. The NLOS assessment function could accurately reflect the attenuation of received signals, and ensure the accuracy of systems under short-term NLOS conditions. The improved system fusion strategy that dynamically adjusts the noise variance according to the probability of signal attenuation can

provide a robust and accurate positioning trajectory when the UWB signal is blocked in a short period of time by obstacles for indoor navigation applications.

Based on the experiments done to date, the accuracy of the integrated system is acceptable in measuring locations of the moving target. Our future work will be focused on the switching mechanism of seamless positioning system when the long-time misalignment of UWB signal is occurred in more complex cases, and test the effect different obstacles and configuration of the transmitters on the positioning accuracy. Moreover, we will study a complete gait detection system including more acceleration features in a different direction since our integrated systems are vulnerable to the diversity of complex behaviors. Finally, a further set of largescale experiments with complex movements in more complex indoor environments is planned to clarify the practical applications of the integrated system.

## VI. REFERENCES

- [1]. L. Chen, E.H. Wu, and M. Jin, "Intelligent fusion of Wi-Fi and inertial sensor-based positioning systems for indoor pedestrian navigation," *IEEE Sensors J.*, vol. 14, no. 11, pp. 4034-4042, Nov. 2014.
- [2]. V. Moreno, M.A. Zamora, and A.F. Skarmeta, "A low-cost indoor localization system for energy sustainability in smart buildings," *IEEE Sensors J.*, vol. 16, no. 9, pp. 3246-3262, May. 2016.
- [3]. A. Yassin, Y. Nasser, and M. Awad, "Recent Advances in Indoor Localization: A Survey on Theoretical Approaches and Applications". *IEEE Commun. Surv. Tut.*, vol. 19, no. 2, pp. 1327-1346, Apr. 2016.
- [4]. A. Momtaz, F. Behnia, and R. Amiri, "NLOS identification in range-based source localization: statistical approach," *IEEE Sensors J.*, vol. 18, no. 9, pp. 3745-3751, May. 2018.
- [5]. Q. Zeng, J. Wang, and Q. Meng, "Seamless pedestrian navigation methodology optimized for indoor/outdoor detection," *IEEE Sensors J.*, vol. 18, no. 1, pp. 363-374, Jan. 2018.
- [6]. R. Harle, "A survey of indoor inertial positioning systems for pedestrians," *IEEE Commun. Surv. Tut.*, vol. 15, no. 3, pp. 1281-1293, Jul. 2013.
- [7]. A. Nordine, Z. Kasmir, and J. Blankenbach, "Step detection for ZUPT-aided inertial pedestrian navigation system using foot-mounted permanent magnet," *IEEE Sensors J.*, vol. 16, no. 17, pp. 6766-6773, Sep. 2016.
- [8]. H. Yin, H. Guo, X. Deng, "Pedestrian Dead Reckoning Indoor Positioning with Step Detection based on foot-mounted IMU," in *Proc Int. Conf. Ins. Nav.*, Nashville, America, Jun. 2014, pp. 186-192.
- [9]. L. Hsu, Y. Gu, and Y. Huang, "Urban pedestrian navigation using smartphone-based dead reckoning and 3-D map-aided GNSS," *IEEE Sensors J.*, vol. 16, no. 5, pp. 1281-1293, Mar. 2016.
- [10]. H. Zhang, W. Yuan, and Q. Shen, "A handheld inertial pedestrian navigation system with accurate step modes and device poses recognition," *IEEE Sensors J.*, vol. 15, no. 3, pp. 1421-1429, Mar. 2015.
- [11]. E.D. Luis, B. Alfonso, and O. Jon, "Step length estimation methods based on inertial sensors: A review," *IEEE Sensors J.*, vol. 18, no. 17, pp. 6908-6926, Sep. 2018.
- [12]. F.S. Muhammad, S. Zoran, and I.W. Kevin, "A novel accelerometer-based technique for robust detection of walking direction," *IEEE Trans. Biomed. Eng.*, vol. 65, no. 8, pp. 1740-1747, Aug. 2018.
- [13]. X. Tao, X. Zhang, and F. Zhu, "Precise displacement estimation from time-differenced carrier phase to improve PDR performance," *IEEE Sensors J.*, vol. 18, no. 20, pp. 8238-8246, Oct. 2018.
- [14]. M. Susi, V. Renaudin, and G. Lachapelle, "Motion mode recognition and step detection algorithms for mobile phone users," *Sensors*, vol. 13, no. 2, pp. 1539-1562, Feb. 2013.
- [15]. Q.L. Tian, Z.S. Zoran, and I.W. Kevin, "A multi-mode dead reckoning system for pedestrian tracking using smartphones," *IEEE Sensors J.*, vol. 16, no. 7, pp. 2079-2093, Apr. 2016.
- [16]. H.T. Duong, and Y.S. Suh, "Walking parameters estimation based on a wrist-mounted inertial sensor for a walker user," *IEEE Sensors J.*, vol. 18, no. 20, pp. 8238-8246, Oct. 2018.
- [17]. W. Kang, and Y. Han, "SmartPDR: Smartphone-based pedestrian dead reckoning for indoor localization," *IEEE Sensors J.*, vol. 15, no. 5, pp.

- 2906-2916, May. 2015.
- [18]. H. Ju, S.Y. Park, and C.G. Park, "A smartphone-based pedestrian dead reckoning system with multiple virtual tracking for indoor navigation," *IEEE Sensors J.*, vol. 18, no. 16, pp. 6756-6764, Aug. 2018.
- [19]. W. Zijlstra, and A.L. Hof, "Assessment of spatio-temporal gait parameters from trunk accelerations during human walking," *Gait Posture*, vol. 18, no. 2, pp. 1-10, Jan. 2003.
- [20]. J.S. Hu, K.C. Sun, and C.Y. Cheng, "A kinematic human-walking model for the normal-gait-speed estimation using tri-axial acceleration signals at waist location," *IEEE Trans. Biomed. Eng.*, vol. 60, no. 8, pp. 2271-2279, Mar. 2013.
- [21]. R.W. Levi, T. Judd, and P. Corporation, "Dead reckoning navigational system using accelerometer to measure foot impacts," U.S. Patent 5583776 A, Dec. 10, 1996.
- [22]. S.H. Shin, and C.G. Park, "Adaptive step length estimation algorithm using optimal parameters and movement status awareness," *Med. Eng. Phys.*, vol. 33, no. 9, pp. 1064-1071, Nov. 2011.
- [23]. Y. Song, S. Shin, and S. Kim, "Speed estimation from a tri-axial accelerometer using neural networks," in *Proc. IEEE Int. Conf. Eng. Med. Biol. Soc. (EMBC)*, Lyon, France, Aug. 2007, pp. 7896-7899.
- [24]. H. Vathsangam, A. Emken, and D. Metz, "Toward free-living walking speed estimation using Gaussian process-based regression with on-body accelerometers and gyroscopes," in *Proc. Int. Conf. Pervasive Comput. Technol. Healthcare.*, Munich, Germany, Mar. 2010, pp. 1-8.
- [25]. S. Zihajehzadeh, and E.J. Park, "A Gaussian process regression model for walking speed estimation using a head-worn IMU," in *Proc. IEEE Int. Conf. Eng. Med. Biol. Soc. (EMBC)*, Seogwipo, Korea, Jul. 2017, pp. 2345-2348.
- [26]. J. Trogh, D. Plets, and A. Thielens, "Enhanced indoor location tracking through body shadowing compensation," *IEEE Sensors J.*, vol. 16, no. 7, pp. 2105-2114, Apr. 2016.
- [27]. J. Zuo, S. Liu, and H. Xia, "Multi-phase fingerprint map based on interpolation for indoor localization using iBeacons," *IEEE Sensors J.*, vol. 18, no. 8, pp. 3351-3359, Apr. 2018.
- [28]. Q. Tian, K.I. Wang, and Z. Salicic, "A low-cost INS and UWB fusion pedestrian Tracking System," *IEEE Sensors J.*, vol. 19, no. 10, pp. 3733-3740, May. 2019.
- [29]. L. Shi, Y. Wang, and G. Liu, "A fusion algorithm of indoor positioning based on PDR and RSS fingerprint," *IEEE Sensors J.*, vol. 18, no. 23, pp. 9691-9698, Dec. 2018.
- [30]. S.S. Saab, and Z.S. Nakad, "A standalone RFID indoor positioning system using passive tags," *IEEE Trans. Ind. Electron.*, vol. 58, no. 5, pp. 1961-1970, May. 2011.
- [31]. P.K. Yoon, S. Zihajehzadeh, and B. Kang, "Robust biomechanical Model-based 3-D indoor localization and tracking method using UWB and IMU," *IEEE Sensors J.*, vol. 17, no. 4, pp. 1084-1096, Feb. 2017.
- [32]. L. Yang and G.B. Giannakis, "Ultra-wideband communications: An idea whose time has come," *IEEE Signal Process. Mag.*, vol. 21, no. 6, pp. 26-54, Nov. 2004.
- [33]. J. Liao, and B. Chen, "Robust Mobile Location Estimator with NLOS Mitigation using Interacting Multiple Model Algorithm," *IEEE T Wirel Commun.*, vol. 5, no. 10, pp. 3002-3006, Nov. 2006.
- [34]. W. M. Gifford, H. Wymeersch, and M. Z. Win, "NLOS Identification and Mitigation for Localization based on UWB Experimental Data," *IEEE J Sel Area in Comm.*, vol. 28, no. 7, pp. 1026-1035, Aug. 2010.
- [35]. Z. Xiao, H. Wen, and A. Markham, "Non-Line-of-Sight Identification and Mitigation Using Received Signal Strength," *IEEE T Wirel Commun.*, vol. 14, no. 3, pp. 1689-1702, May. 2015.
- [36]. H. Wymeersch, S. Marano, and W. M. Gifford, "A Machine Learning Approach to Ranging Error Mitigation for UWB Localization," *IEEE T Commun.*, vol. 60, no. 6, pp. 1719-1728, Feb. 2012.
- [37]. X. Yang, "NLOS mitigation for UWB localization based on sparse pseudo-input Gaussian process," *IEEE Sensors J.*, vol. 18, no. 10, pp. 4311-4316, May. 2018.
- [38]. P.D. Groves, "Navigation using inertial sensors [Tutorial]," *IEEE Aerosp. Electron. Syst. Mag.*, vol. 30, no. 2, pp. 42-69, Feb. 2015.
- [39]. J.A. Corrales, F.A. Candelas, and F. Torres, "Sensor data integration for indoor human tracking," *Robot. Auto. Syst.*, vol. 58, no. 8, pp. 931-939, Aug. 2010.
- [40]. J. Lu, K. Chen, and B. Li, "Hybrid navigation method of INS/PDR based on action recognition," *IEEE Sensors J.*, vol. 18, no. 20, pp. 8541-8548, Oct. 2018.
- [41]. Q. Fan, Y. Wu, and J. Hui, "Integrated navigation fusion strategy of INS/UWB for indoor carrier attitude angle and position synchronous tracking," *Sci. World J.*, vol. 2014, pp. 1-13, Jul. 2014.
- [42]. X. Li, Y. Wang, and K. Khosheham, "UWB/PDR Tightly Coupled Navigation with Robust Extended Kalman Filter for NLOS Environments," *Mob Inf Syst.*, vol. 2018, pp. 1-14, May. 2018.
- [43]. X. Li, Y. Wang, and K. Khosheham, "A Robust and Adaptive Complementary Kalman Filter Based on Mahalanobis Distance for Ultra Wideband/Inertial Measurement Unit Fusion Positioning," *Sensor.*, vol. 18, no. 3435, pp. 3501-3522, Oct. 2018.
- [44]. Y. Xu, C. K. Ahn, and Y. S. Shmaliy, "Adaptive Robust INS/UWB Integrated Pedestrian Tracking using UFIR Filter Bank," *Measurement.*, vol. 123, no. 1, pp.1-7, Nov. 2018.
- [45]. Q. Fan, B. Sun, and Y. Sun, "Performance enhancement of MEMS-based INS/UWB integration for indoor navigation applications," *IEEE Sensors J.*, vol. 17, no. 10, pp. 3116-3130, May. 2017.
- [46]. H. Weinberg. (2002). *Using the ADXL202 in pedometer and personal navigation applications*. Accessed: Jun. 11, 2018. [Online]. Available: <http://www.t-es-t.hu/download/analog/an602.pdf>
- [47]. J. Scarlett. (Mar. 2007). *Enhancing the performance of pedometers using a single accelerometer*. Accessed: Jun. 11, 2018. [Online]. Available: <http://www.analog.com/cn/analog-dialogue/articles/enhancing-pedometers-using-single-accelerometer.html>.
- [48]. V. Savic, J. Ferrer-Coll, and P. Angskog, "Measurement Analysis and Channel Modeling for TOA-Based Ranging in Tunnels," *IEEE T Wire Commun.*, vol. 14, no. 1, pp. 456-467, May. 2015.
- [49]. DecaWave. (2017). *DW1000 user manual*. Accessed: Jul. 15, 2019. [Online]. Available: <https://www.decawave.com/dw1000/usermanual/>
- [50]. C. Hyunmin, and K. Younggoo, "RSS-based indoor localization with PD R location tracking for wireless sensor networks," *Int. J. Electron. Commun.*, vol. 70, no. 15, pp. 250-256, Dec. 2015.
- [51]. P. Chen, Y. Kuang, and X. Chen, "A UWB/improved PDR integration algorithm applied to dynamic indoor positioning for pedestrians," *Sensors*, vol. 17, no. 9, pp. 90-109, Sep. 2017.
- [52]. Z. Li, G. Chang, and J. Gao, "GPS UWB MEMS-IMU tightly coupled navigation with improved robust Kalman filter," *Adv Space Res.*, vol. 58, no. 3, pp. 2424-2434, Jul. 2016.